Computational Modelling of Ankle-Foot Orthosis to Evaluate Spatially Asymmetric Structural Stiffness: Importance of Geometric Nonlinearity

Wataru Sumihira[1], Tomohiro Otani[1], Yo Kobayashi[1], Masao Tanaka[1]

1. Department of Mechanical Science and Bioengineering, Graduate School of Engineering Science, Osaka University, Toyonaka, Osaka, Japan

Corresponding author:

Tomohiro Otani, PhD

Affiliation: Department of Mechanical Science and Bioengineering, Graduate School of Engineering Science, Osaka University

Full Mailing Address: 1-3 Machikaneyamacho, Toyonaka, Osaka 560-8531, Japan

Email: otani.tomohiro.es@osaka-u.ac.jp

Phone: +81-6-6850-6174

Fax: None

Keywords: AFO, buckling, large deflection, dorsiflexion, corotational triangle element

ABSTRACT

An ankle-foot orthosis (AFO) constructed as a single piece of isotropic elastic material is a commonly used assistive device that provides stability to the ankle joint of patients with spastic diplegic cerebral palsy. The AFO has asymmetric stiffness that restricts plantarflexion during the swing phase while it is flexible to allow dorsiflexion during the stance phase with a large deflection, including buckling originating from geometric nonlinearity. However, its mechanical implications have not been sufficiently investigated. This study aims to develop a computational model of an AFO considering geometric nonlinearity and examine AFO stiffness asymmetry during plantarflexion and dorsiflexion using physical experiments. Three-dimensional AFO mechanics with geometric nonlinearities were expressed using corotational triangle-element formulations that obeyed Kirchhoff–Love plate theory. Computational load tests for plantarflexion and dorsiflexion, using idealized AFOs with two different ankle-region designs (covering or not covering the apexes of the malleoli), showed that plantarflexion moment–ankle angle relationships were linear and dorsiflexion moment–ankle angle relationships were nonlinear; increases in dorsiflexion led to negative apparent stiffness of the AFO. Both ankle-region designs resisted both plantarflexion and dorsiflexion, and out-of-plane elastic energy was locally concentrated on the lateral side, resulting in large deflections during dorsiflexion. These findings give insight into appropriate AFO design from a mechanical viewpoint by characterizing three-dimensional structural asymmetry and geometric nonlinearity.

1. INTRODUCTION

An ankle-foot orthosis (AFO) designed from a single piece of lightweight thermoformable isotropic elastic material is an external assistive device commonly used to provide stability to the ankle joint of individuals with spastic diplegic cerebral palsy impaired gait [1–3]. An AFO covers the posterior lower leg and sole of the foot [4] to prevent the foot from dropping during mid and terminal swing phases [5–7], and thus, the AFO must restrict plantarflexion during the swing phase. However, the AFO should be sufficiently flexible to allow dorsiflexion during the stance phase, which is important for smooth forward progression in a normal gait[5]. Clinicians customize the AFO design for patients to provide appropriate spatially asymmetric structural stiffness (i.e., apparent AFO stiffness depending on the deformation states) [8,9]. Furthermore, recent advances in additive manufacturing allow for the flexible design of AFOs for each patient, not limited to the trimline adjustment [10,11]. From these perspectives, a detailed understanding of the mechanical characteristics of the AFO can provide valuable insight into the mechanically appropriate AFO design for each patient.

AFO design and asymmetry of the structural stiffness with buckling behaviour during plantarflexion and dorsiflexion have been demonstrated experimentally [8,9,12–14]. Bregman et al. [15] showed that the buckling of AFOs during dorsiflexion occurred in the functional range of motion of the ankle during the gait in physical experiments. This asymmetric structural stiffness of the AFO originated from geometric nonlinearity via a large deflection (finite deformation) in a mechanical sense. Here, geometric nonlinearity is a source of nonlinearity in solid analyses, such as buckling, and important when changes in

geometry have a significant effect on the load-deformation behaviour [16]. However, previous studies mainly determined the stiffness of a custom AFO (for an individual patient) within a linear range of deformation using a small (infinite) deformation theorem. As a result, little is known about the structural mechanical design of AFOs and asymmetric nonlinear stiffness. Therefore, a better understanding of the asymmetric nonlinear mechanical properties in structural AFO design is valuable.

To clarify the mechanical characteristics of AFO designs for individual patients before physical construction, computational simulation has been found to be a useful approach [17,18]. In recent studies, computational simulation has been used to evaluate stiffness or stress–strain characteristics in AFO designs with realistic conditions [19] and material properties [20]. However, the effects of geometric nonlinearity on the mechanics of AFOs have only been studied by Syngellakis et al. [21], to the best of our knowledge. Syngellakis et al. [21] reported that AFO stiffness in dorsiflexion appeared to be greater than that in plantarflexion and that their findings contradicted experimental evidence from previous studies [8,9,12–14]. Geometric nonlinearity and associated asymmetric stiffness of AFOs have been recognized in clinical practice, but the implications of these characteristics with respect to AFO functionality have not been sufficiently considered.

This study aims to develop a computational model of an AFO to express its asymmetric structural stiffness during plantarflexion and dorsiflexion. We examined the mechanical responses of the AFO from external loading during plantarflexion and dorsiflexion based on physical experiments[15] to gain insight into the effects of geometric nonlinearity on the mechanical behaviours. AFO mechanical assumptions were based on Kirchhoff–Love

plate theory, and three-dimensional equilibrium states with large deflection is precisely obtained by the idea of corotational triangle element formulation. In this formulation, large deflection of the plate can be treated as separately divided into small deformation on the local coordinate system assigned at each triangle element and finite rotation of the local coordinate system independently. Thus, geometric nonlinearity originating from finite rotation can be considered. We conducted case studies using idealized AFOs with two different ankle-region designs.

2. Methods

2.1 AFO design

Two idealized AFO designs were created based on the shape of a human left lower leg and foot (heel to toe length: 27 cm; archived in GrabCAD; https://grabcad.com/library/scanned-human-foot-and-leg-1) (Fig. 1 (a)). We constructed a smooth surface based on the foot model using a surface fitting tool of Autodesk Fusion 360 (Autodesk Inc. San Rafael, CA, USA) (Fig. 1(b)). The anterior region was cut and modified to cover the upper calf, based on the designs of AFOs used in clinical practice identified by a discussion with a physical therapist familiar with gait rehabilitation. Two ankle designs were created—one where the apexes of the malleoli were covered (design A) and one where the apexes of the malleoli were not covered (design B)—for a case study of different AFO designs (Fig. 1(c) and (d)).

2.2 Computational modelling

2.2.1 Mechanical model

The AFO was modelled as a thin smooth plate with constant thickness [22], based on Kirchhoff plate theory. Unit orthogonal axes $(\mathbf{r}_1 \quad \mathbf{r}_2 \quad \mathbf{r}_3)$ are assigned as a local coordinate system, where $\mathbf{r}_1$ and $\mathbf{r}_2$ are tangential unit vectors, and $\mathbf{r}_3$ is a unit vector normal to the plate. The plate deformation in the local coordinate system is measured by the infinitesimal strain tensor $\boldsymbol{\varepsilon}$ in Voigt notation, given by

$$\boldsymbol{\varepsilon} = \begin{pmatrix} \varepsilon_{11} & \varepsilon_{22} & 2\varepsilon_{12} \end{pmatrix}^{\cdot} = \begin{pmatrix} \frac{\partial u_{\mathrm{L},1}}{\partial x_1} & \frac{\partial u_{\mathrm{L},2}}{\partial x_2} & \frac{\partial u_{\mathrm{L},1}}{\partial x_2} + \frac{\partial u_{\mathrm{L},2}}{\partial x_1} \end{pmatrix}^{\cdot}, \tag{1}$$

and the curvature vector $\boldsymbol{\kappa}$, given by

$$\boldsymbol{\kappa} = \begin{pmatrix} \kappa_1 & \kappa_2 & 2\kappa_{12} \end{pmatrix}^{\cdot} = \begin{pmatrix} \frac{\partial \theta_{\mathrm{L},1}}{\partial x_1} & \frac{\partial \theta_{\mathrm{L},2}}{\partial x_2} & \frac{\partial \theta_{\mathrm{L},2}}{\partial x_1} + \frac{\partial \theta_{\mathrm{L},1}}{\partial x_2} \end{pmatrix}^{\cdot}, \tag{2}$$

where $\mathbf{u}_{\mathrm{L}} \in \square^3$ and $\boldsymbol{\theta}_{\mathrm{L}} \in \square^3$ are transitional and rotational displacement vectors in the local coordinate system, respectively. The elastic energy U of the plate is the sum of in-plane elastic energy U_{in}, from stretching and compression, and out-of-plane elastic energy U_{out}, from bending:

$$U = U_{\mathrm{in}} + U_{\mathrm{out}}. \tag{3}$$

U_{in} and U_{out} are surface integrals defined as

$$U_{\mathrm{in}} = \frac{1}{2}\int_{\Omega} h\boldsymbol{\varepsilon}^{\text{封}}\mathbf{D}\boldsymbol{\varepsilon} d\Omega, \; U_{\mathrm{out}} = \frac{1}{2}\int_{\Omega} \frac{h^3}{12}\boldsymbol{\kappa} \; \mathbf{D}\boldsymbol{\kappa} d\Omega, \tag{4}$$

where Ω is the plate area, h is the thickness, and the linear elastic constitutive matrix under plane stress

$$\mathbf{D} = \frac{E}{1-\nu^2}\begin{pmatrix} 1 & \nu & 0 \\ \nu & 1 & 0 \\ 0 & 0 & \frac{1-\nu}{2} \end{pmatrix}, \tag{5}$$

is defined by the plate material's Young's modulus E and Poisson's ratio ν.

2.2.2 Discretization

The AFO is discretized as a set of three-node triangular elements with 18 degrees of freedom $\mathbf{d}_{\mathrm{L}} = \begin{bmatrix} \mathbf{u}_{\mathrm{L}}^1 & \boldsymbol{\theta}_{\mathrm{L}}^1 & \mathbf{u}_{\mathrm{L}}^2 & \boldsymbol{\theta}_{\mathrm{L}}^2 & \mathbf{u}_{\mathrm{L}}^3 & \boldsymbol{\theta}_{\mathrm{L}}^3 \end{bmatrix}$, where the superscript number shows the node number of a triangle element as shown in Fig. 2. As described by Battini and Pacoste [23], the in-plane stiffness matrix was derived from U_{in} using the optimal membrane triangle-element formulation [24], and the out-of-plane (bending) stiffness matrix was derived from U_{out} using the discrete Kirchhoff triangle-element formulation [25–27]. To integrate these stiffness matrixes, stress resultants $\mathbf{f}_{\mathrm{L}} \in \mathbb{R}^{18}$ in the local coordinates system can be given as

$$\mathbf{f}_{\mathrm{L}} = \mathbf{K}_{\mathrm{L}}\mathbf{d}_{\mathrm{L}}, \tag{6}$$

where $\mathbf{K}_{\mathrm{L}} \in \mathbb{R}^{18\times 18}$ is the stiffness matrix constant in the local coordinate system assigned to each triangular element.

We used the corotational triangle-element formulation developed in [23,28–31] to precisely define geometric nonlinearity in large deflections. Stress resultants in the global coordinate system $\mathbf{f}_{\mathrm{G}} \in \mathbb{R}^{18}$ can be obtained by the coordinate transformation $\mathbf{f}_{\mathrm{G}} = \mathbf{B}\mathbf{f}_{\mathrm{L}}$, where $\mathbf{B} \in \mathbb{R}^{18\times 18}$ is the coordinate transformation matrix. To obtain mechanical

equilibrium state under external loading $\mathbf{f}_{\text{ext}} \in \mathbb{R}^{18}$, we solved the static equilibrium equation

$$\mathbf{f}_{\text{G}}\left(\mathbf{d}_{\text{G}}\right) + \mathbf{f}_{\text{ext}} = \mathbf{0} \tag{7}$$

with respect to translational and rotational displacements $\mathbf{d}_{\text{G}} \in \mathbb{R}^{18}$ for each node in the global coordinate system using the Newton–Raphson method. For more details of this formulation and implementation, please see [30].

The linear system equation from eq. (7) was calculated using PARDISO implemented in the Intel Math Kernel Library. To treat instable behaviour of the AFO after buckling, the displacement control scheme was adapted. Verification of the code implementation was performed by solving a benchmark test (Appendix 1).

2.3 Simulation

AFO material properties were set to correspond to those of polypropylene (E = 1 GPa and $\nu = 0.35$), and the thickness of the AFO was set to 2 mm [21]. Triangle elements were created by Meshmixer 3.5.474 (Autodesk Inc. San Rafael, CA) with total number of triangular elements were 7,259 and 6,918 in designs A and B, respectively. The mesh size dependency of the solutions was analysed by comparing them to a solution derived using a finer mesh (22,065 elements) in design A. For the load test shown in the results section, the maximum difference of the resulting moment of the simulations with two different mesh sizes was lower than 2%. Thus, we concluded that the mesh size used in this study was acceptable.

For the load test, we set the plane formed by *y* and *z* unit orthogonal axes coincident to the AFO's midsagittal plane; the top of the calf was set to y=0, and the sole of the foot was set to z=0 (Fig. 3(a)). Translational and rotational displacements constraints at the sole of the foot (z=0) were fixed. Relationships between moments of the AFO around the axis normal to the *y*-*z* plane (at the defined origin) and ankle angles from 10° plantarflexion to 20° dorsiflexion were obtained, representing the functional range of the ankle during gait [32]. In this computation, a displacement control scheme [33] was adapted to treat the unstable post-buckling behaviour of the AFO. The prescribed displacement associated with the above ankle angle was applied midplane to the AFO corresponding to the top of the calf region for plantarflexion and dorsiflexion, and a resultant moment was obtained as a reaction. In addition, we considered the effects internal and external rotation on apparent stiffness of the AFO, given that internal and external rotations (±10°) occur during plantarflexion and dorsiflexion [34]. We set the internal/external rotation angle range from −10° (external) to 10° (internal) in 5°-increments in the load test (Fig. 3(b)).

3. Results

During plantarflexion, resulting moments linearly increased with increasing plantarflexion angle for both designs (Fig. 4). Moments for design A were greater than those of design B. During dorsiflexion, resulting moment increases with increasing dorsiflexion angle were not monotonic; the apparent stiffness of the AFO (steepness of the curve's tangent) became negative at a flexion angle of approximately 5° for both

designs. Snapshots of the dorsiflexion load test (Fig. 4 (bottom)) show large deflections occurred at the lateral side the AFO near the ankle region; midsurface deformation of the AFO was spatially asymmetric. Differences due to the internal and external rotation of the AFO were negligible during plantarflexion but slightly noticeable near the local maximum of the AFO moment during dorsiflexion.

To interpret AFO mechanical characteristics during plantarflexion and dorsiflexion, we evaluated the in-plane and out-plane elastic energies (U_{in} and U_{out}) stored in the AFO (Fig. 5). During plantarflexion, the in-plane elastic energies were relatively higher than the out-plane elastic energies. In contrast, during dorsiflexion, the out-plane elastic energies were higher than the in-plane elastic energies. These tendencies were shown in both design A and design B; however, the elastic energy of design A was consistently higher than that of design B regardless of the loading direction.

Spatial distributions of in-plane and out-of-plane elastic energy were illustrated (Fig. 6). At −10° (plantarflexion), in-plane elastic energy was higher than out-of-plane energy, and there were local maximums along the AFO trimline, especially near the ankle region of the design A. At 20° (dorsiflexion), in-plane elastic energy was lower than that at −10°, and out-of-plane energy was concentrated on the lateral side of the AFO near the ankle region, where large deflections occurred.

4. Discussion

In the present study, we examined AFO structural stiffness during plantarflexion and dorsiflexion, taking geometric nonlinearity into account. The moment–angle relationship was linear during plantarflexion but nonlinear during dorsiflexion, and apparent AFO

stiffness became negative during dorsiflexion, with large deflections on the lateral side of the AFO (Fig. 4). Buckling found in our study was consistent with findings from a previous study [15] for corresponding ranges of moments and ankle angles, demonstrating that asymmetric AFO structural stiffness occurs as a result of geometric nonlinearity during dorsiflexion. From a clinical viewpoint, this buckling behaviour can be interpreted to provide high flexibilities of the AFO during dorsiflexion. These results suggest that the mechanical evaluations of the nonlinear behaviours with large deflection may be used to consider the clinically relevant mechanical characteristics of the AFO.

The AFO trimline, especially in the ankle region, is of primary interest in clinical practice when considering AFO design adjustments to modify stiffness [8,35]. Our results showed that relatively high amounts of elastic energy were stored in the AFO near the ankle region during both plantarflexion and dorsiflexion (Fig. 6). During plantarflexion, relatively high amounts of in-plane elastic energy were found along the trimline of design A which indicates that the AFO structure near the ankle performs mechanical work to resist plantarflexion through in-plane elastic stiffness. During dorsiflexion, relatively high amounts of out-of-plane elastic energy were stored in the AFO's lateral side (Fig. 6). Bending of the AFO on the lateral side caused mechanical instability (buckling)—a state with a negative apparent stiffness (Fig. 4). These findings highlight the different mechanical roles of AFO trimline design during plantarflexion or dorsiflexion. For clinical use, AFO trimline designs that allow high in-plane elastic stiffness and low stiffness to counter small bending loads may provide sufficient stiffness during plantarflexion and flexibility during dorsiflexion. Although physicians may consider these mechanical

implications empirically in their design process, this detailed characterization of AFO mechanical function may be valuable for systematic AFO design , which is useful in the field of additive manufacturing with 3-D printers [36,37].

During plantarflexion and dorsiflexion, ankle kinematics include internal and external rotations (approximately ±10°, with subject-specific differences[34]). This complex joint motion occurs because the functional axis of the ankle joint is not perpendicular to the sagittal plane[38]. These characteristics were not taken into account when AFO stiffness was evaluated by applying an external load or moment in the midsagittal plane (e.g., in [15]). In this study, the effects of internal and external rotation on AFO stiffness were considered and did not have a noticeable effect, especially within the linear range of deformation (Fig. 4 top-left). Based on these findings, the assumptions used in previous studies appear to be appropriate for evaluating linear stiffness. In contrast, the effects of the internal and external rotations were evident near the local maximum of the resultant moment (Fig. 4 top-right). Although these differences may be secondary from clinical viewpoints, this finding suggests that geometric nonlinearity of the AFO should be taken into account to comprehensively characterize AFO mechanics.

Three limitations of the study were identified. First, in this study, simplifications of AFO designs and mechanical properties were used. Although these simplifications make interpretation of the effects of geometric nonlinearity easier, quantitative evaluations of AFO stiffness and changes under external loads are more difficult. For example, this study assumed that the AFO thickness was constant, whereas the AFO thickness is not constant in the adjustment process and may be an influential factor in the AFO mechanical

behaviours. Second, the boundary conditions applied in this study do not fully reflect actual conditions of the human gait; instead they were set based on physical experiments of the AFO stiffness during uniaxial rotation[15]. The results can clarify fundamental AFO mechanical characteristics with geometric nonlinearity and its local mechanical states; however, the AFO stiffness obtained from simplified boundary conditions does not correspond to actual usage with non-uniaxial rotation. Further considerations using personalized computational conditions and the validations based on physical AFO experiments would be valuable in the mechanically appropriate AFO design for each patient. Third, load tests were conducted using two AFO designs. An additional systematic study using other AFO designs, such as parametric studies about the trimline and thickness, are necessary for a detailed understanding of the AFO design from a mechanical viewpoint and for a mechanically appropriate AFO design for each patient.

5. Conclusions

The present study demonstrated a computational model of AFO considering geometric nonlinearity and investigated AFO structural stiffness during plantarflexion and dorsiflexion. Resulting moment–ankle angle relationships were linear during plantarflexion, with predominantly in-plane elastic stiffness performing mechanical work. Resulting moment–ankle angle relationships during dorsiflexion were nonlinear due to bending and buckling of the lateral side of the AFO. These findings demonstrated asymmetric structural stiffness of the AFOs during plantarflexion and dorsiflexion as well as geometric nonlinearity of the AFOs during dorsiflexion. The proposed computational

model enables the expression of the fundamental mechanical behaviours of AFO with geometric nonlinearity. Thus, we believe that the model can be used as a base computational model for mechanically appropriate AFO design considering patient-specific conditions.

Acknowledgments

We thank Tatsuya Arakawa, PT, PhD, for input on clinical matters and discussions on the AFO model creation. We thank Coren Walters-Stewart, PhD, from Edanz (https://jp.edanz.com/ac) for editing a draft of this manuscript.

Funding

This work was supported by a research grant from Japan Society for the Promotion of Science (JSPS) Grants-in-Aid for Early-Career Scientists (18H18367).

Declaration of conflicting interests

The Authors declare that there is no conflict of interest.

Appendix 1. Code verification

Verification of the code implemented for corotational triangular elements was conducted as a benchmark for nonlinear large deformation (*c.f.*, [30,39]). An isotropic cylinder was fully fixed at one end and free at the other end. The radius, length, and thickness of the cylinder were set to 1.016, 3.048, and 0.03, respectively, and the Young's

modulus and Poisson's ratio were set to 2.0685×10^7 and 0.3, respectively. The cylinder was discretized using 32×16 triangular elements, and a vertical load was applied to the surface of the free end (Fig. A1 (top)). Figure A1 (bottom) shows the load–displacement curve at the loading point. Our results and those of Battini [30], who originally proposed the corotational triangular element used in this study, were in excellent agreement, and thus, we concluded that our implementation successfully passed the benchmark test.

REFERENCES

1. Kobayashi T, Singer ML, Orendurff MS, et al. The effect of changing plantarflexion resistive moment of an articulated ankle-foot orthosis on ankle and knee joint angles and moments while walking in patients post stroke. *Clin Biomech* 2015; 30: 775–780.
2. Holtkamp F, Wouters E, van Hoof J, et al. Use of and Satisfaction with Ankle Foot Orthoses. *Clin Res Foot Ankle* 2015; 3: 167.
3. Tyson SF, Kent RM. Effects of an ankle-foot orthosis on balance and walking after stroke: A systematic review and pooled meta-analysis. *Arch Phys Med Rehabil* 2013; 94: 1377–1385.
4. Daryabor A, Arazpour M, Aminian G. Effect of different designs of ankle-foot orthoses on gait in patients with stroke: A systematic review. *Gait Posture* 2018; 62: 268–279.
5. Õunpuu S, Bell KJ, Davis RB, et al. An evaluation of the posterior leaf spring orthosis using joint kinematics and kinetics. *J Pediatr Orthop* 1996; 16: 378–384.
6. Smiley SJ, Jacobsen FS, Mielke C, et al. A comparison of the effects of solid, articulated, and posterior leaf-spring ankle-foot orthoses and shoes alone on gait and energy expenditure in children with spastic diplegic cerebral palsy. *Orthopedics* 2002; 25: 411–415.
7. Buckon CE, Thomas SS, Jokobson-Huston S, et al. Comparison of three ankle-foot orthosis configurations for children with spastic diplegia. *Dev Med Child Neurol* 2004; 46: 590–598.

8. Sumiya T, Suzuki Y, Kasahara T. Stiffness control in posterior-type plastic ankle-foot orthoses: Effect of ankle trimline. Part 2: Orthosis characteristics and orthosis/patient matching. *Prosthet Orthot Int* 1996; 20: 132–137.

9. Sumiya T, Suzuki Y, Kasahara T. Stiffness control in posterior-type plastic ankle-foot orthoses: Effect of ankle trimline. Part 1: A device for measuring ankle moment. *Prosthet Orthot Int* 1996; 20: 129–131.

10. Chen RK, Jin Y an, Wensman J, et al. Additive manufacturing of custom orthoses and prostheses-A review. *Addit Manuf* 2016; 12: 77–89.

11. Leite M, Soares B, Lopes V, et al. Design for personalized medicine in orthotics and prosthetics. *Procedia CIRP* 2019; 84: 457–461.

12. Condie DN, Meadows CB. Some biomechanical considerations in the design of ankle-foot orthoses. *Orthot Prosthetics* 1977; 31: 45–52.

13. Nagaya M. Shoehorn-type ankle-foot orthoses: Prediction of flexibility. *Arch Phys Med Rehabil* 1997; 78: 82–84.

14. Cappa P, Patanè F, Di Rosa G. A continuous loading apparatus for measuring three-dimensional stiffness of ankle-foot orthoses. *J Biomech Eng* 2005; 127: 1025–1029.

15. Bregman DJJ, Rozumalski A, Koops D, et al. A new method for evaluating ankle foot orthosis characteristics: BRUCE. *Gait Posture* 2009; 30: 144–149.

16. Bonet J, Gil A, Wood R. *Nonlinear Solid Mechanics for Finite Element Analysis: Statics*. Cambridge: Cambridge University Press., 2016. Epub ahead of print 2016. DOI: 10.1017/CBO9781316336144.

17. Ielapi A, Forward M, De Beule M. Computational and experimental evaluation of the mechanical properties of ankle foot orthoses: A literature review. *Prosthet Orthot Int* 2019; 43: 339–348.

18. Lee YS, Choi YJ, Kim HS, et al. A study on the structural stress analysis of plastic ankle foot orthosis (AFO) under dorsiflexion and plantarflextion conditions. *Int J Mod Phys B* 2006; 20: 4559–4564.

19. Jamshidi N, Hanife H, Rostami M, et al. Modelling the interaction of ankle-foot orthosis and foot by finite element methods to design an optimized sole in steppage gait. *J Med Eng Technol* 2010; 34: 116–123.

20. Faustini MC, Neptune RR, Crawford RH, et al. Manufacture of passive dynamic ankle-foot orthoses using selective laser sintering. *IEEE Trans Biomed Eng* 2008; 55: 784–790.

21. Syngellakis S, Arnold MA, Rassoulian H. Assessment of the non-linear behaviour of plastic ankle foot orthoses by the finite element method. *Proc Inst Mech Eng Part H J Eng Med* 2000; 214: 527–539.

22. International Committee of the Red Cross's Physical Rehabilitation Programme. *Manufacturing Guidelines Ankle-Foot Orthosis*. 2012.

23. Battini JM, Pacoste C. On the choice of the linear element for corotational triangular shells. *Comput Methods Appl Mech Eng* 2006; 195: 6362–6377.

24. Felippa CA. A study of optimal membrane triangles with drilling freedoms. *Comput Methods Appl Mech Eng* 2003; 192: 2125–2168.

25. Batoz J, Bathe KJ, Ho LW. A sstudy of three-node trianglar plate bending elements. *Int J Numer Methods Eng* 1980; 15: 1771–1812.

26. Batoz JL. An explicit formulation for an efficient triangular plate-bending element. *Int J Numer Methods Eng* 1982; 18: 1077–1089.

27. Jeyachandrabose C, Kirkhope J, Babu CR. An alternative explicit formulation for the DKT plate-bending element. *Int J Numer Methods Eng* 1985; 21: 1289–1293.

28. Pacoste C. Co-rotational flat facet triangular elements for shell instability analyses. *Comput Methods Appl Mech Eng* 1998; 156: 75–110.

29. Eriksson A, Pacoste C. Element formulation and numerical techniques for stability problems in shells. *Comput Methods Appl Mech Eng* 2002; 191: 3775–3810.

30. Battini JM. A modified corotational framework for triangular shell elements. *Comput Methods Appl Mech Eng* 2007; 196: 1905–1914.

31. Battini JM, Pacoste C. On the choice of local element frame for corotational triangular shell elements. *Commun Numer Methods Eng* 2004; 20: 819–825.

32. Perry J, Burnfield JM. *Gait Analysis, Normal and Pathological Function.* second edi. SLACK, 2010. Epub ahead of print 2010. DOI: 10.2106/00004623-199303000-00027.

33. Borst R de, Crisfield MA, Remmers JJ, et al. *Nonlinear Finite Element Analysis of Solids and Structures*. 2nd ed. Chichester: John Wiley & Sons, Ltd, 2012.

34. de Asla RJ, Wan L, Rubash HE, et al. Six DOF in vivo kinematics of the ankle joint complex: Application of a combined dual-orthogonal fluoroscopic and magnetic resonance imaging technique. *J Orthop Res* 2006; 24: 1019–27.

35. Bielby SA, Warrick TJ, Benson D, et al. Trimline severity significantly affects rotational stiffness of ankle-foot orthosis. *J Prosthetics Orthot* 2010; 22: 204–210.

36. Ielapi A, Vasiliauskaite E, Hendrickx M, et al. A novel experimental setup for evaluating the stiffness of ankle foot orthoses. *BMC Res Notes* 2018; 11: 1–7.

37. Ielapi A, Lammens N, Van Paepegem W, et al. A validated computational framework to evaluate the stiffness of 3D printed ankle foot orthoses. *Comput Methods Biomech Biomed Engin* 2019; 22: 880–887.

38. Van den Bogert AJ, Smith GD, Nigg BM. In vivo determination of the anatomical axes of the ankle joint complex: an optimization approach. *J Biomech* 1994; 27: 1477–1488.

39. Balah M, Al-Ghamedy HN. Finite element formulation of a third order laminated finite rotation shell element. *Comput Struct* 2002; 80: 1975–1990.

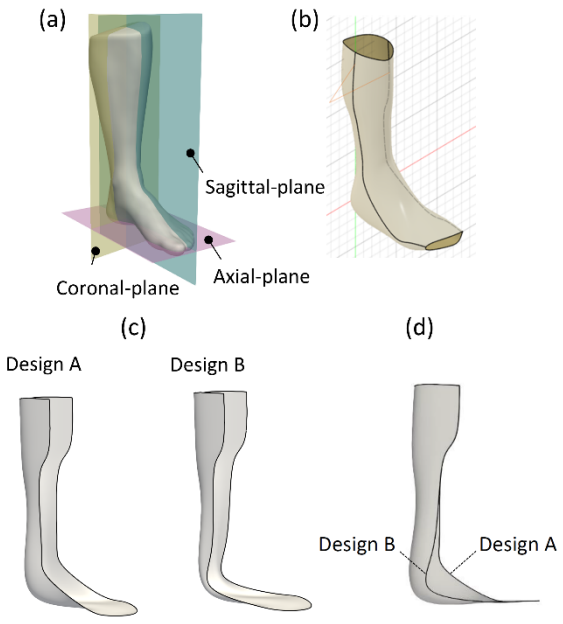

Fig. 1 AFO model construction overview. (a) A smooth cylindrical surface based on a human left foot was created. (b) The anterior side of the cylindrical surface was cut. (c) Two designs covering and not covering the apexes of the malleoli were constructed (designs A and B). (d) Lateral views of these designs.

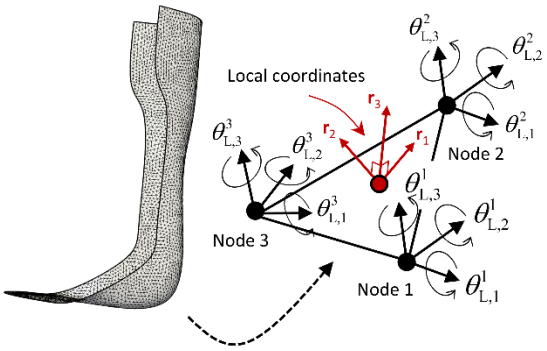

Fig. 2 Schematic of the computational model of the AFO. The AFO is discretized as sets of three-node triangular elements. A local coordinate system is assigned to each element, and an orthonormal triad is set for each node. A node thus has three-dimensional translational and rotational freedom of movement.

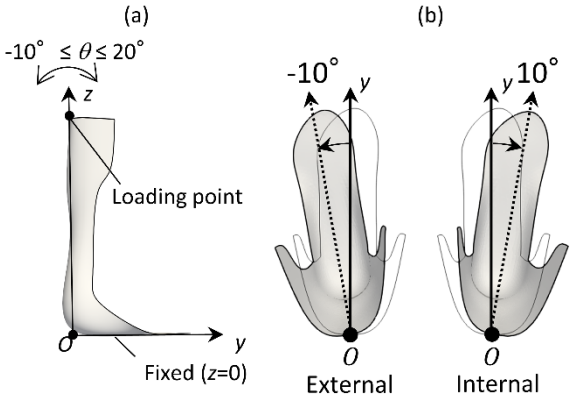

Fig. 3 Setup of the load test during plantarflexion and dorsiflexion: (a) boundary conditions and (b) internal and external rotations of the AFO.

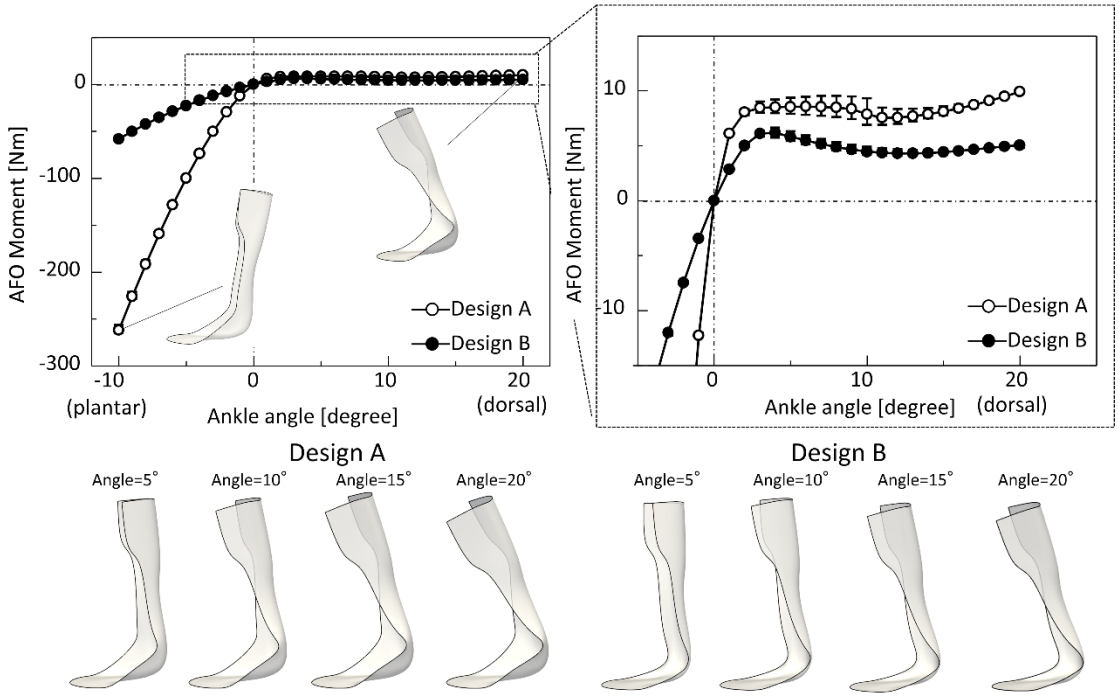

Fig. 4 AFO moment–ankle angle relationships of designs A and B during plantarflexion and dorsiflexion (top). Snapshots of the AFO designs A and B (transparent view) during simulated dorsiflexion of the model (bottom). Error bars show maximum and minimum values for external/internal rotation angles (n=5, from −10° to 10° in 5°-increments).

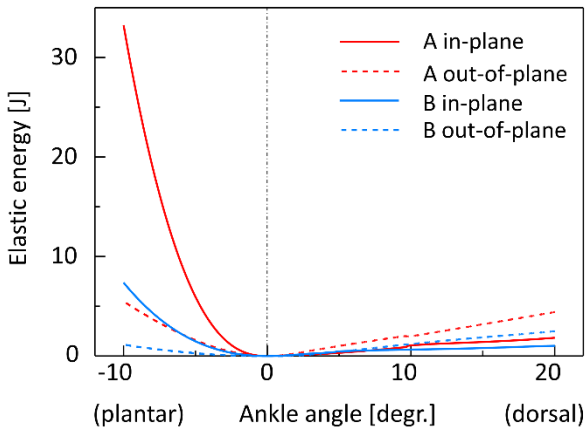

Fig. 5 Elastic energy–ankle angle relationships for designs A (red) and B (blue) during plantarflexion and dorsiflexion, with 0° of external/internal rotation. Solid and dashed lines show in-plane and out-of-plane elastic energies, respectively.

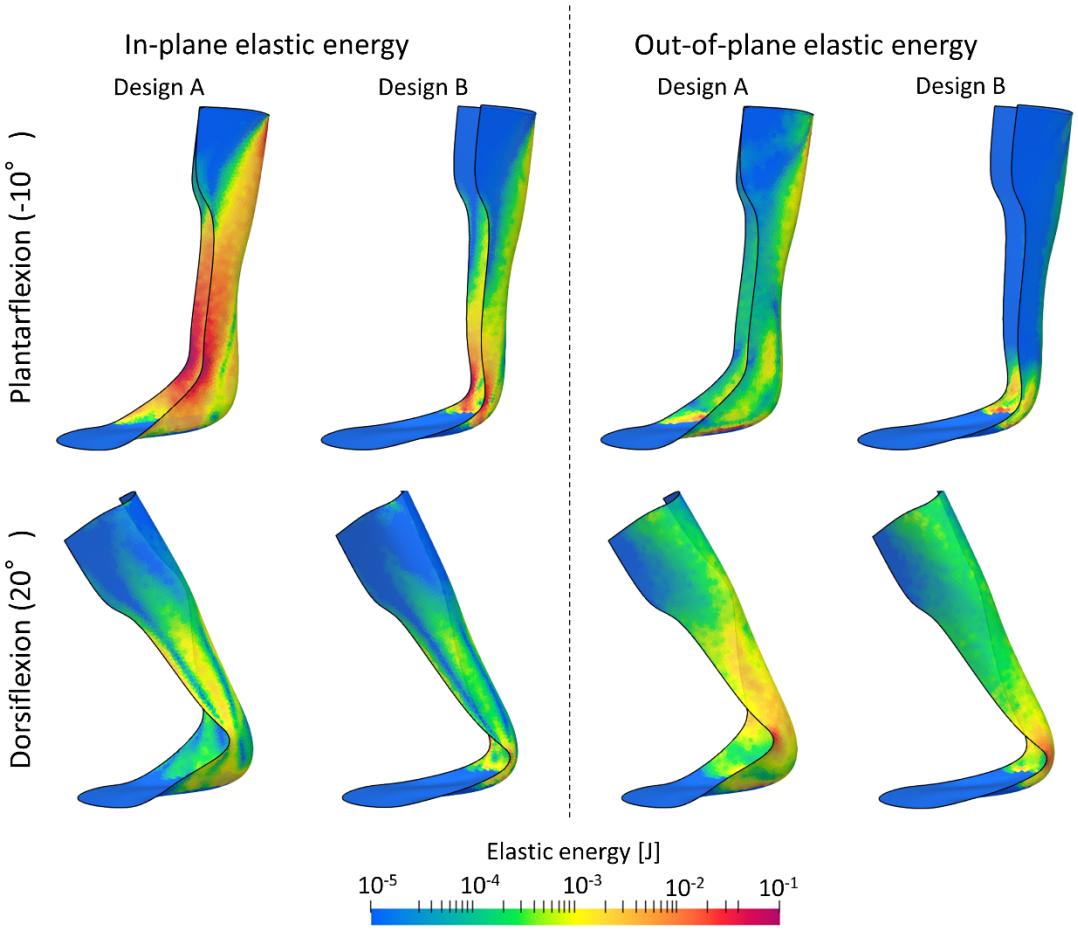

Fig. 6 Spatial distributions of the in-plane and out-of-plane elastic energy at −10° (plantarflexion, top) and 20° (dorsiflexion, bottom), with 5° of external/internal rotation, for designs A (left) and B (right).

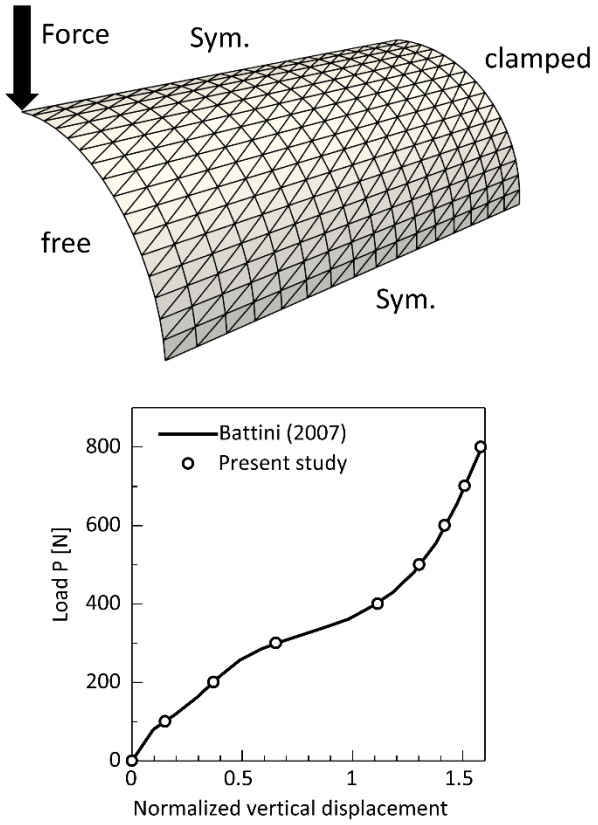

Fig. A1 Pinching of a clamped cylinder (top) and load–vertical displacement curve at the application point (bottom). Vertical displacement was normalized by the radius of the cylinder.